energies

MDPI

Communication

Influence of Calcination Temperature on Electrochemical Properties of Perovskite Oxide Nanofiber Catalysts

Ji-Woo Park [1], Jeeyoung Shin [2,3,*] and Young-Wan Ju [1,4,*]

[1] Department of Chemical Engineering, College of Engineering, Wonkwang University, Iksan 54538, Republic of Korea; wldnro4612@naver.com
[2] Department of Mechanical Systems Engineering, Sookmyung Women's University, Seoul 04310, Republic of Korea
[3] Institute of Advanced Materials and Systems, Sookmyung Women's University, Seoul 04310, Republic of Korea
[4] ICT Fusion Green Energy Research Institute, Wonkwang University, Iksan 54538, Republic of Korea
* Correspondence: jshin@sookmyung.ac.kr (J.S.); ywju1978@wku.ac.kr (Y.-W.J.)

Abstract: Energy conversion and storage systems have recently attracted significant attention owing to increasing environmental and energy problems. However, the slow kinetics of the oxygen reduction reaction (ORR) and the oxygen evolution reaction (OER) render their commercialization difficult. Many studies are being conducted to replace precious metal catalysts that have high activity for the ORR and OER but have scarcity and low stability. In this study, $Sm_{0.5}Sr_{0.5}CoO_3$ (SSC) nanofibers were fabricated via the electrospinning of non-precious metal-based perovskite oxides to replace precious metal catalysts. In addition, the properties and electrochemical performance of SSC fibers synthesized at different calcination temperatures were evaluated. The small crystallite size, high specific surface area, abundant oxygen vacancies, and high ORR/OER activity suggest that SSC800 hollow fibers are optimal bifunctional catalysts.

Keywords: calcination; electrospinning; oxygen reduction reaction (ORR); oxygen evolution reaction (OER); perovskite oxide

check for updates

Citation: Park, J.-W.; Shin, J.; Ju, Y.-W. Influence of Calcination Temperature on Electrochemical Properties of Perovskite Oxide Nanofiber Catalysts. *Energies* **2023**, *16*, 4979. https://doi.org/10.3390/en16134979

Academic Editors: Yifei Wang, Dennis Y.C. Leung, Xu Lu and Hao Zhang

Received: 30 May 2023
Revised: 13 June 2023
Accepted: 26 June 2023
Published: 27 June 2023

Copyright: © 2023 by the authors. Licensee MDPI, Basel, Switzerland. This article is an open access article distributed under the terms and conditions of the Creative Commons Attribution (CC BY) license (https://creativecommons.org/licenses/by/4.0/).

1. Introduction

Metal-air batteries and fuel cells are attracting attention as the most effective and efficient systems to address the current environmental and energy problems [1–5]. Although these energy conversion and storage systems are environmentally friendly and have a high energy density, their commercialization is limited owing to the sluggish kinetics of the oxygen reduction reaction (ORR) and the oxygen evolution reaction (OER) [6–8]. Pt- and Ir-based catalysts are excellent electrochemical catalysts for the ORR and OER [9–11]. However, because precious metals are scarce, less stable, and expensive, many research groups have focused on developing bifunctional catalysts for non-precious metals [12–14].

Several materials, including carbon-based materials [15–17] and transition metal oxides [18–20], are promising candidates for bifunctional electrocatalysts and can replace precious metal catalysts [21,22]. However, owing to the low activity and durability of carbon-based materials for the OER, many studies have focused on transition metal oxide (TMO) catalysts [23,24]. Among the TMOs, perovskite-structured metal oxides are promising candidates because they can be easily synthesized at a relatively low cost. Furthermore, they provide an excellent model for the rational design of bifunctional catalysts because of their unique electronic, ionic, magnetic, catalytic, and environmentally friendly properties [25–27].

Perovskites have the chemical formula ABO_3, and examples include $LaNiO_3$ [28], $LaCoO_3$ [29], and $La_{1-x}Sr_xMnO_3$ [30]. Usually, site A comprises rare earth or alkaline

earth metals, and site B comprises transition metals [31]. Bu et al. reported perovskite-structured $Sm_{0.5}Sr_{0.5}CoO_3$ (SSC) as a potential bifunctional catalyst owing to its low cost, environmental friendliness, and favorable chemical, physical, and catalytic properties (e.g., high ionic and electronic conductivities and a fast oxidation exchange) [32]. Conventional methods such as the sol–gel method [33,34], the hydrothermal method [35,36], the co-precipitation method [37], and the electrospinning [38–40] method can be used to synthesize perovskite oxide nanomaterials [41]. Because the adsorption and dissociation of oxygen molecules occur mainly at the surface and interface of the catalyst during the ORR and OER, it is essential to synthesize nanomaterials with high specific surface areas to improve the electrode catalyst activity [42,43]. Hence, nanofibers synthesized through the simple and cost-effective electrospinning method have attracted considerable attention because of their high specific surface area and tunable 1D fiber structure [44].

In this study, a perovskite-structured SSC with a large specific surface area was synthesized with electrospinning. The morphology, specific surface area, and oxygen vacancies of the SSC nanofibers were examined at various calcination temperatures (973–1273 K). Based on these characteristics, the bifunctional electrochemical catalytic activities of the ORR and OER were investigated. Our results suggest that a small crystallite size is related to a large specific surface area, abundant oxygen vacancies, and improved ORR and OER performances.

2. Materials and Methods

2.1. Synthesis of SSC Nanofibers via Electrospinning

SSC nanofibers were fabricated via electrospinning. Cosolvent containing deionized water, ethanol, and acetic acid (Sigma-Aldrich, 99%) was used in a volume ratio of 1:1:3 to prepare a 0.1 M SSC solution. $Sm(NO_3)_3 \cdot 6H_2O$ (Alfa Aesar, 99.9%), $Sr(NO_3)_2$ (Samchun Chemical, 98%), and $Co(NO_3)_2 \cdot 6H_2O$ (Samchun Chemical, 97%) were used as the precursors. A 10 wt.% electrospinning solution was prepared by stirring the prepared stock solution with the addition of polyvinylpyrrolidone (PVP; MW = ~1,300,000 g/mol, Sigma-Aldrich) for 10 h. The applied voltage was 18 kV; the distance between the nozzle tip and collector was 15 cm, and the solution supply rate was 1 mL/h. The SSC nanofibers obtained after electrospinning were calcined in air for 3 h over a temperature range of 973–1273 K. The SSC nanofibers were named SSC700, SSC800, SSC900, and SSC1000 according to the calcination temperatures of 973 K, 1073 K, 1173 K, and 1273 K, respectively.

2.2. Characterization

The crystal structures of the samples were analyzed with X-ray diffraction (XRD; MiniFlex600, Rigaku, Tokyo, Japan) using Cu-Kα radiation over a 2θ range of 20–80°. Field-emission scanning electron microscopy (FE-SEM; S-4800, Hitachi, Tokyo, Japan) was used to examine the shape and structure of the synthesized fiber samples. The specific surface area, pore volume, pore size distribution, and pore morphology of the samples were analyzed from the N_2 adsorption/desorption isotherms at 77 K using the Brunauer–Emmett–Teller equation (BET; BELSORP-mini II, MicrotracBEL, Osaka, Japan). The binding energies for O 1s and Co 2p were analyzed with X-ray photoelectron spectroscopy (XPS; Thermo ESCALAB 250, Thermo Fisher, Waltham, MA, USA) using Al-Kα radiation. The electrochemical activities of the ORR and OER were evaluated using a rotating ring-disk electrode (RRDE; RRDE-3A, ALS, Tokyo, Japan). The ORR and OER were performed in 0.1 M KOH; Hg/HgO(1 M NaOH) was used as the reference electrode, and a Pt wire was used as the counter electrode. A glassy carbon disk was used as the working electrode. An electrocatalyst ink was prepared by adding 20 mg of samples to a volume ration of 0.45:0.45:0.1 ethanol, IPA, and Nafion solution. After sonication of the prepared electrocatalyst ink for 30 min, 5 µL of electrocatalyst ink was loaded and dried at room temperature. The ORR was measured over a range of −0.8 to 0.2 V, while the OER was measured over a range of 0.3 to 1.0 V. The scan rates for the ORR and OER were 10 and 30 mV/s, respectively. Measurements were performed in an O_2 atmosphere after 20 min of N_2 purging.

3. Results and Discussion

Figure 1 shows the XRD patterns of the SSC nanofibers calcined over a temperature range of 973–1273 K. The XRD patterns of all samples showed diffraction peaks corresponding to the perovskite oxide $Sm_{0.5}Sr_{0.5}CoO_3$ (JCPDS No. 53-0112). Diffraction peaks corresponding to pure SSC were observed in all SSC nanofiber samples except SSC700. The SSC700 sample exhibited typical perovskite oxide diffraction peaks and additional peaks corresponding to impurities such as Co_3O_4 (JCPDS No. 09-0418), SrO_2 (JCPDS No. 01-1113), Sr (JCPDS No. 01-0574), and Sm_2O_3 (JCPDS No. 15-0813). The crystal structure of SSC was less formed at a low calcination temperature of 973 K, and diffraction peaks that corresponded to impurities were observed. As shown in Figure S3, the SSC750 sample calcined at 1023 K also shows that a SrO_2 diffraction peak exists as an impurity other than the pure SSC diffraction peak. This suggests that a minimum calcination temperature of 1073 K is required to fabricate SSC nanofibers. Except for SSC700, which contained impurities, the XRD intensity increased with increasing calcination temperature. The crystallite size was calculated from the XRD patterns using Scherrer's equation:

$$D = \frac{0.94\lambda}{\beta \times \mathrm{Cos}\theta}$$

Here, D is the crystallite size, λ is the X-ray wavelength, β is the full width at half maximum, and θ is the diffraction angle. The crystallite size was calculated from the XRD diffraction peak of 33°, the main peak of SSC. Calculating the crystallite size of SSC700 was difficult owing to impurities; the crystallite sizes of SSC800, SSC900, and SSC1000 were 14.57, 22.25, and 22.78 nm, respectively. The crystallite size increased with increasing calcination temperature. Several studies have reported that smaller crystallites contain more oxygen vacancies [45] and exhibit improved ORR performance [18]. Therefore, SSC800, composed of a pure SSC phase with a small crystallite size, was expected to have the maximum number of oxygen vacancies and the best ORR performance.

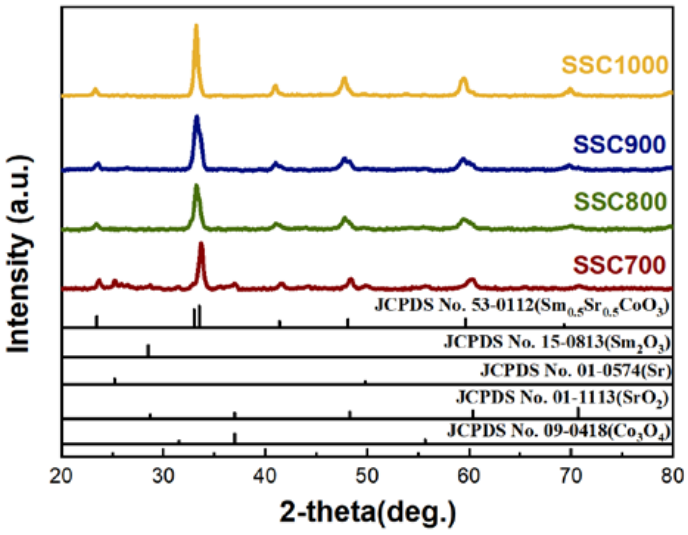

Figure 1. XRD patterns of perovskite oxide SSC samples calcined at 973–1273 K.

FE-SEM analysis was performed to confirm the fiber diameter and shape of the SSC nanofibers calcined over a temperature range of 973–1273 K. Figures 2 and 3 show the FE-SEM images of the SSC nanofibers at low and high magnifications, respectively. The low-magnification FE-SEM images of SSC800 (Figure 2b) indicate a porous structure, whereas those of SSC700 (Figure 2a), SSC900 (Figure 2c), and SSC1000 (Figure 2d) indicate a solid and dense shape. The diameters of most of the synthesized fibers were in the range of 160–330 nm. The SEM images show that the average diameter decreased with increasing calcination temperature. In the Figure S4, SSC750 did not show a porous structure like

SSC700, and SSC850 shows a dense shape structure as the calcination temperature increased. SSC800 (Figure 3b-1) exhibited a porous structure with hollow fiber, as evident from the high-magnification FE-SEM image. However, the SSC700 fibers showed a solid shape at low calcination temperatures. The SSC fibers synthesized at a low temperature of 973 K underwent less progressive polymer decomposition. Consequently, residual carbon formed and hindered the particle growth, and SSC700 looks like a dense shape. To confirm the presence of residual carbon, we performed an EDS analysis (Supporting Information). The elemental mapping images of SSC800 indicated the presence of Sm, Sr, Co, and O (Figure S1). However, the elemental mapping images of SSC700 (Figure S2) confirmed the presence of residual carbon through elemental C mapping. Notably, the residual carbon in the nanofibers at low calcination temperatures hindered the formation of hollow fibers. Hollow porous fibers have been shown to exhibit enhanced catalytic activity for the ORR and OER, with abundant active sites and rapid electron/ion/mass pathways [46].

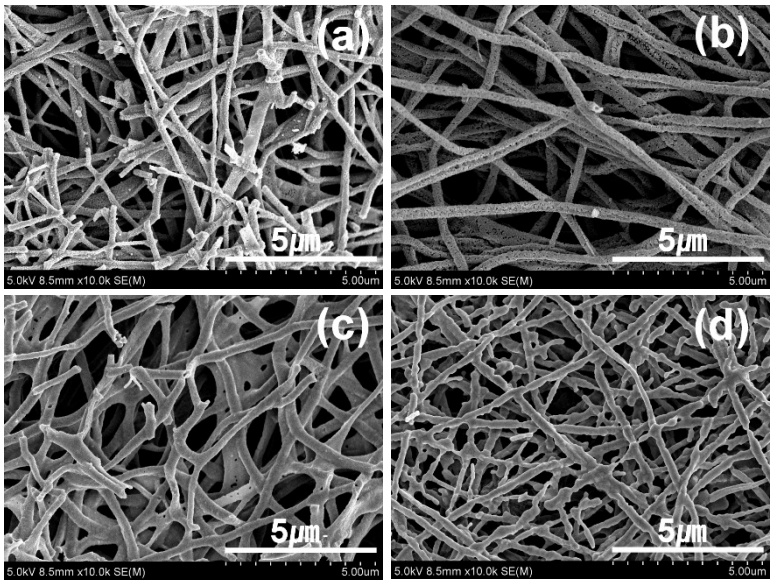

Figure 2. Low magnification FE-SEM images of SSC fibers calcined at (**a**) 973 K, (**b**) 1073 K, (**c**) 1173 K, (**d**) 1273 K.

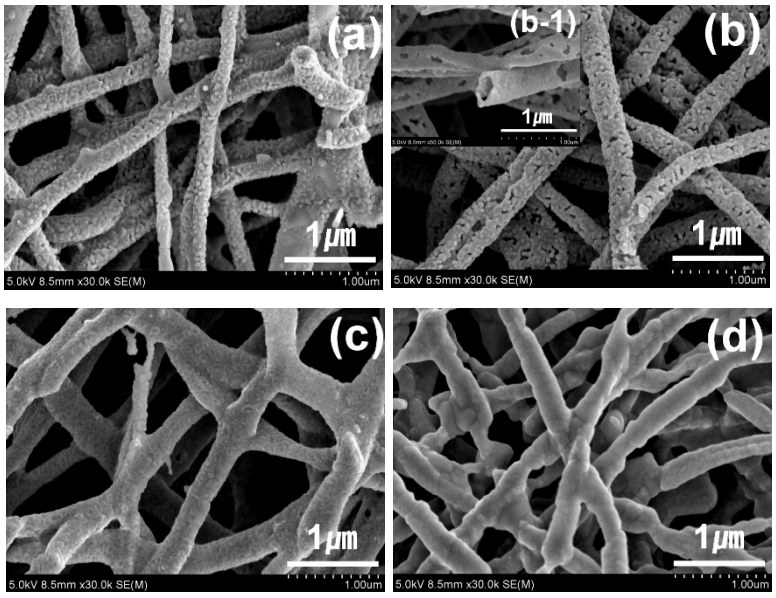

Figure 3. High magnification FE-SEM images of SSC fibers calcined at (**a**) 973 K, (**b**) 1073 K, (**b-1**) 1073 K hollow fiber, (**c**) 1173 K, (**d**) 1273 K.

N_2 adsorption–desorption isotherms were performed to confirm the specific surface area, pore volume, and pore size distribution of the synthesized nanofibers. As shown in Figure 4a, all samples exhibited type IV isotherms with hysteresis loops, indicating the presence of mesopores. The Barrett–Joyner–Halenda pore size distribution (Figure 4b) showed that SSC800 had more mesopores and macropores than the other samples. Table 1 lists the specific surface area, pore volume, and average pore diameter of the SSC fibers calcined at 973–1273 K. As shown in Table 1, SSC700, SSC800, SSC900, and SSC1000 exhibited specific surface areas of 4.15, 7.94, 3.57, and 2.10 m^2/g, respectively. Except for SSC800, all samples exhibited low specific surface areas and average pore diameters with increasing calcination temperature. This was attributed to the grain growth with increasing calcination temperature. SSC800 had a larger specific surface area than SSC700 owing to its porous and hollow structure. SSC700 had a smaller surface area because residual carbon blocked the pores, as shown in Figure 2a. As reported by Chen et al., a high specific surface area provides more active sites for the ORR [47], suggesting that SSC800, with its high specific surface area, should exhibit good ORR activity.

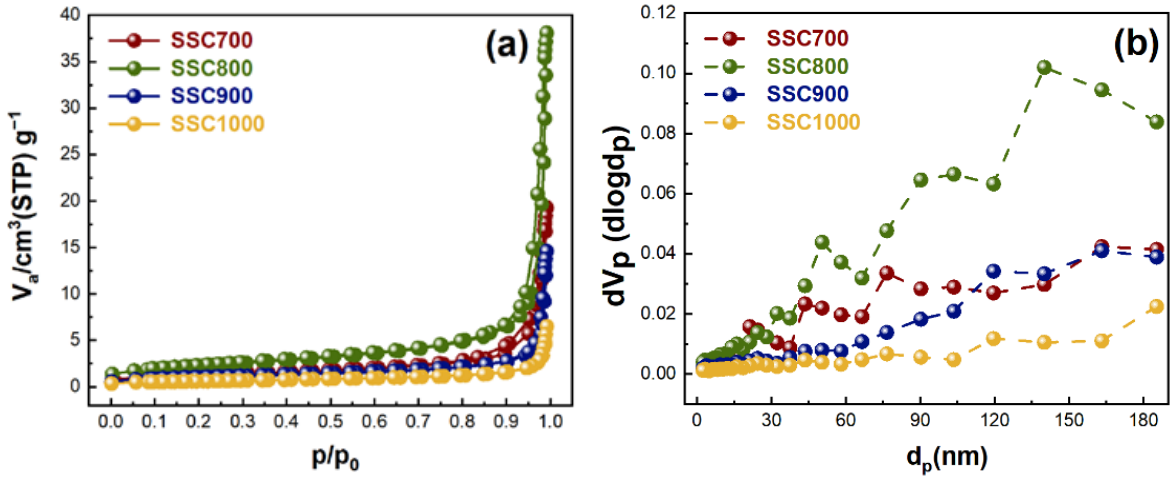

Figure 4. (**a**) Nitrogen adsorption–desorption isotherms of SSC fibers, (**b**) Barrett–Joyner–Halenda (BJH) pore size distribution.

Table 1. The comparison of SSAs, pore volume, and average pore diameter of SSC fibers calcined at 973–1273 K.

Sample	Specific Surface Area (m^2/g)	Pore Volume (cm^3/g)	Average Pore Diameter (nm)
SSC700	4.15	0.027	25.95
SSC800	7.94	0.053	26.51
SSC900	3.57	0.019	21.49
SSC1000	2.10	0.008	15.80

Figures 5 and 6 show the O and Co XPS spectra of the SSC fibers calcined at different temperatures. The O 1s XPS spectra of the synthesized samples confirmed changes in the lattice and adsorbed oxygens. SSC fibers fitted O 1s XPS spectra based on 528.34 eV for O-lattice and 531.1 eV for O-adsorbed. Figure 5 shows the O 1s spectrum for the samples based on the O 1s XPS table, with a slight peak shift depending on the actual measured peak for each sample. The $O_{Adsorbed}/O_{Lattice}$ ratios for SSC700, SSC800, SSC900, and SSC1000 were 5.39, 5.61, 5.33, and 5.20, respectively; the ratios are summarized in Table 2. The number of oxygen vacancies increased in the order of SSC800, SSC700, SSC900, and SSC1000. Figure 6 shows the Co 2p spectra of the SSC fibers calcined at 973–1273 K. As shown in the Co $2p_{1/2}$ spectra, Co^{3+} and Co^{4+} peaks appeared at approximately 779.7 and 781.46 eV, respectively. The Co^{4+}/Co^{3+} ratios in the Co $2p^{1/2}$ spectra of SSC700, SSC800, SSC900, and SSC1000 were 1.012, 0.925, 0.985, and 0.992, respectively. For SSC800, the

ratio was the smallest (0.925), while it was comparatively higher and similar for the other samples. A small Co^{4+}/Co^{3+} ratio indicates a high Co^{3+} content, suggesting the presence of more oxygen vacancies and, thus, enhanced electrical conductivity [48]. The oxygen vacancy and Co^{3+} ratios are proportional. Many oxygen vacancies correlate to the crystallite size calculated based on the XRD patterns [45]. As discussed in the section on XRD analysis, a smaller crystallite size indicates a greater number of oxygen vacancies. Many studies have reported that oxygen vacancies enhance ORR and OER activity [49,50].

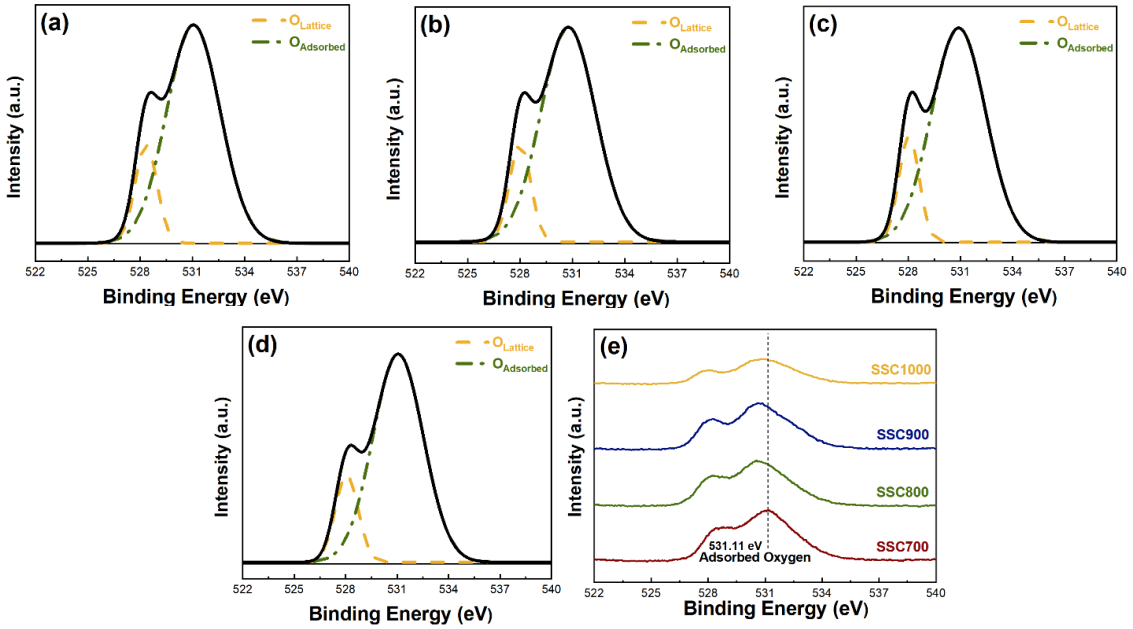

Figure 5. X-ray photoelectron spectrum of O 1s of SSC fibers calcined at (**a**) 973 K, (**b**) 1073 K, (**c**) 1173 K, (**d**) 1273 K, and (**e**) O 1s overall spectrum.

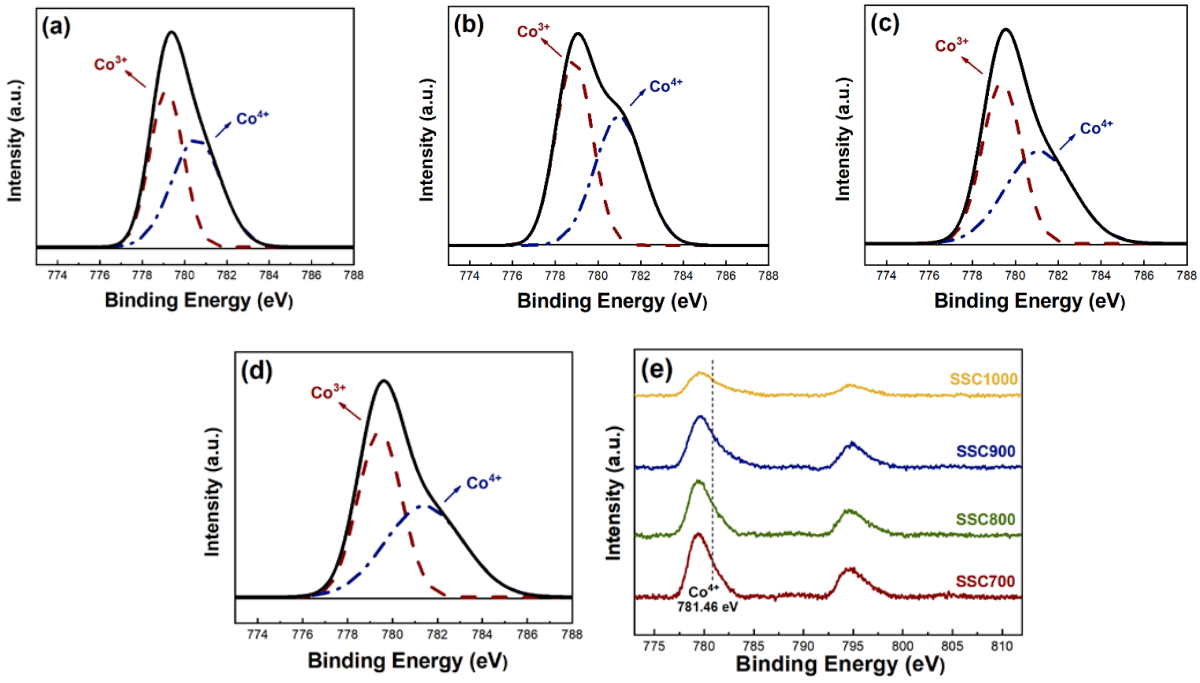

Figure 6. X-ray photoelectron spectrum of Co $2p^{1/2}$ of SSC fibers calcined at (**a**) 973 K, (**b**) 1073 K, (**c**) 1173 K, (**d**) 1273 K, and (**e**) Co 2p overall spectrum.

Table 2. Summary of XPS O 1s, Co 2p spectra ratio of SSC fibers calcined at 973−1273 K.

Sample	O 1s $O_{adsorbed}/O_{Lattice}$	Co 2p Co^{4+}/Co^{3+}
SSC700	5.39	1.012
SSC800	5.61	0.925
SSC900	5.33	0.985
SSC1000	5.20	0.992

The ORR was investigated with linear sweep voltammetry to evaluate the electrochemical activity of the synthesized SSC fibers (Figure 7). Pt/C, which is known to exhibit a high ORR activity, was examined for comparison (Figure 7a). Pt/C exhibited a high activity and current density of -4.19 mA·cm^{-2} at -0.8 V and a limited current density of -4 mA·cm^{-2} at -0.25 V. The current density, which is affected by the geometric surface of the electrode, is related to the specific surface area. A higher specific surface area provides more active sites for the ORR, resulting in higher current densities [47,51]. As proven by many studies, SSC800, SSC700, SSC900, and SSC1000 were confirmed to exhibit high current density values in the order of specific surface area values. The SSC700, SSC800, SSC900, and SSC1000 fibers showed onset potentials of -0.233, -0.222, -0.252, and -0.265 V, respectively. SSC800 showed excellent ORR activity and achieved the highest current density (-3.54 mA·cm^{-2}) and lowest onset potential (-0.222 V). Notably, the hollow SSC800 fiber with a porous structure shows high ORR activity by enhancing the surface oxygen exchange reaction area, attributed to the high specific surface area and presence of oxygen vacancies [47,50]. Figure 7b shows the electron transfer number of the ORR. The electron transfer number (n) was determined through the equation below.

$$n = 4 \times \frac{I_D}{I_D + (I_R/N)}$$

Here, I_D is the disk current, I_R is the ring current, N (=0.42) is ring collection efficiency. Values close to four were observed for all SSC fibers at all temperatures, and, except for Pt/C, the reaction in the presence of SSC800 most resembled a four-electron reaction. This resulted in a fast and efficient reduction reaction owing to the low overpotential for the direct reduction of O_2 to H_2O [52].

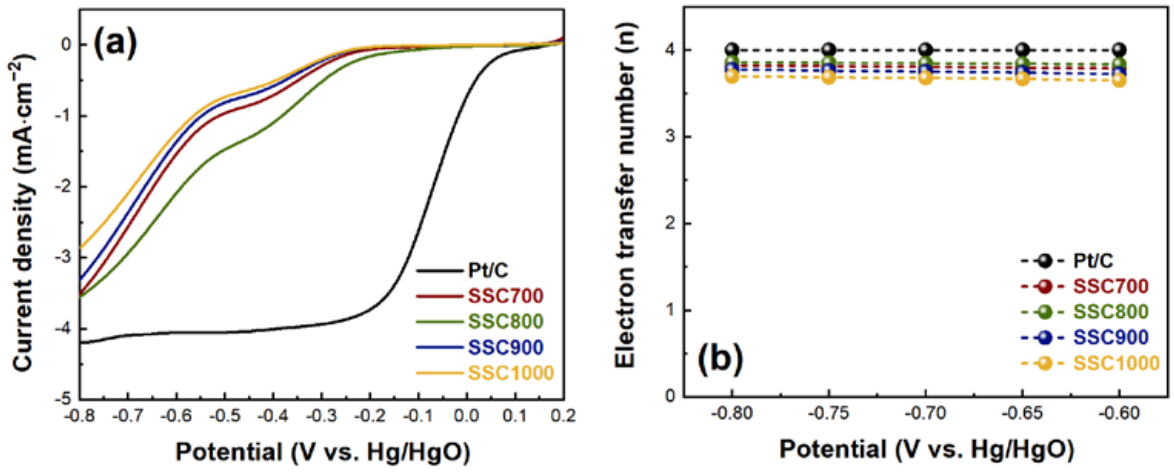

Figure 7. (**a**) Linear sweep voltammograms (LSV) for ORR curves and (**b**) Electron transfer number.

To evaluate the electrochemical activity of the synthesized SSC fibers, the OER was investigated with linear sweep voltammetry (Figure 8). For comparison, the OER was investigated under the same conditions (Figure 8a) in the presence of IrO_2, which is known to exhibit high OER activity. The SSC fibers showed higher OER activity than IrO_2 at all calcination temperatures, and the onset potentials of IrO_2, SSC700, SSC800, SSC900, and

SSC1000 for the OER were 0.759, 0.742, 0.732, 0.743, and 0.761 V, respectively. SSC800, SSC700, SSC900, SSC1000, and IrO_2 showed the lowest onset potential values in the order. As shown in Figure 8b, it was confirmed with the overpotential of the E_{RHE} value measured at the value of current density 10 mA·cm^{-2}. Figure S5 shows the OER curve with the potential values corrected using the formula $E_{RHE} = E_{Hg/HgO} + 0.059\ pH + E^{\circ}_{Hg/HgO}$. At a current density of 10 mA·cm^{-2}, IrO_2, SSC700, SSC800, SSC900, and SSC1000 showed an overpotential of 1.82, 1.69, 1.67, 1.70, and 1.73 V, respectively. Notably, SSC800 exhibited the lowest overpotential, followed by SSC700, SSC900, and SSC1000. Thus, SSC800 showed high catalytic activity, as well as a low onset potential and overpotential for the OER. Similarly to the ORR, the better OER performance was attributed to the large specific surface area and abundant oxygen vacancies owing to the increased surface activity of the hollow fibers.

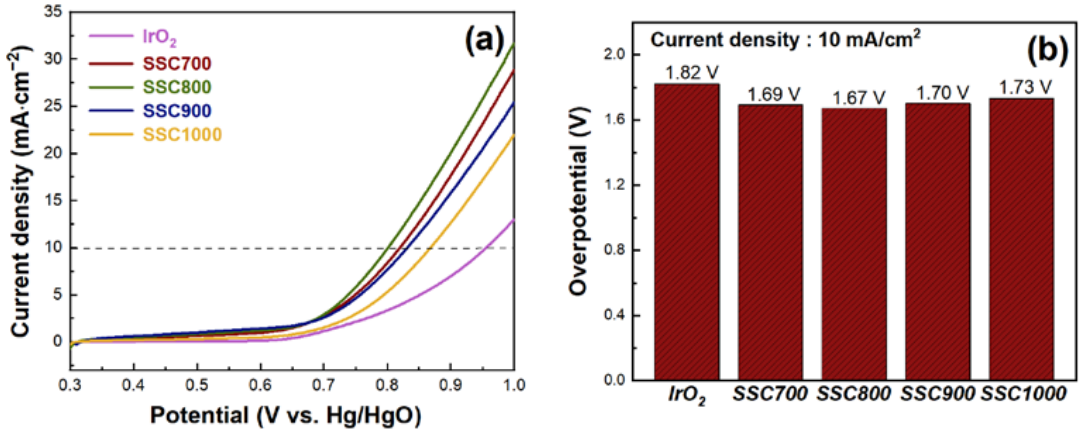

Figure 8. (**a**) Linear sweep voltammograms (LSV) for OER curves and (**b**) OER overpotential values at the same current density of 10 mA/cm^2.

Figure 9 shows a graph evaluating the ORR/OER stability of the SSC800 sample, which has bifunctional catalyst activity for ORR/OER. The stability test was measured under the same conditions of each ORR and OER, and stability was evaluated with a graph after 3000 cycles. ORR and OER show almost similar activities after each 3000 cycles. In addition, after 3000 cycles, ORR decreased by 5.6% and OER by 2%, and it was confirmed that SSC showed excellent stability of ORR/OER. This excellent stability suggests that the sample properties of the electrocatalyst remain intact even after electrolysis. SSC800 is suitable as a bifunctional electrocatalyst due to its high activity for ORR and OER as well as excellent stability.

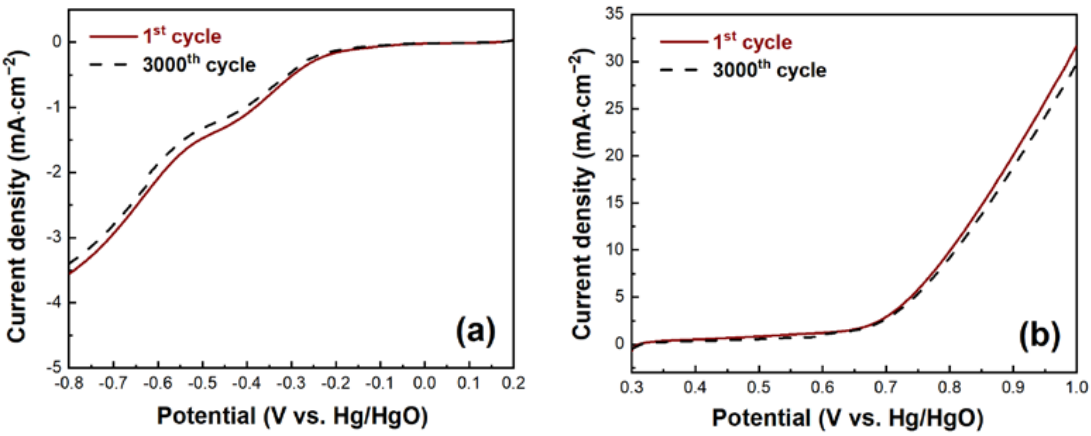

Figure 9. Stability test of SSC800: (**a**) ORR curve after 3000 cycles, (**b**) OER curve after 3000 cycles.

4. Conclusions

In this study, SSC nanofibers were fabricated via electrospinning and calcined at different temperatures. The perovskite phase and fiber shape were confirmed with XRD and SEM analyses. The XRD patterns indicated that the SSC fibers calcined at the lowest temperature contained impurities. SEM and EDS analyses confirmed that the less advanced polymer decomposition produced residual carbon and looked like a dense structure of the fibers. A pure SSC phase was formed at a calcination temperature of 1073 K, as confirmed by the XRD patterns. Moreover, at calcination temperatures of 1173 and 1273 K, a dense shape with a low specific surface area was obtained owing to the growth of large crystal grains. We suggest SSC800 synthesized at a calcination temperature of 1073 K as an optimal catalyst. As confirmed with SEM, the SSC800 fibers had a hollow and porous structure. The small crystallite size (14.57 nm) and porous morphology of SSC800 provide abundant active sites, leading to the formation of a large number of oxygen vacancies and a high specific surface area (7.9353 m^2/g). We confirmed that the ORR and OER performances improved owing to abundant active sites and fast electron/ion pathways. SSC800 also shows high stability for ORR/OER after 3000 cycles. Therefore, we conclude that the small crystallite size in the SSC800 sample confers a large specific surface area and abundant oxygen vacancies, thereby improving the ORR and OER performances.

Supplementary Materials: The following supporting information can be downloaded at: https://www.mdpi.com/article/10.3390/en16134979/s1, Figure S1: SSC fibers calcined at 1073 K (a) EDS image, (b) EDS mappings of Sm(red), Sr(pink), Co(yellow), O(white); Figure S2: SSC fibers calcined at 973 K (a) EDS image, (b) EDS mappings of Sm(red), Sr(pink), Co(yellow), O(white), C(green); Figure S3: XRD patterns of perovskite oxide SSC750, SSC850; Figure S4: FE-SEM images of SSC fibers of (a) SSC750 (b) SSC850; Figure S5: Linear sweep voltammograms (LSV) for OER curves of corrected the potential value E_{RHE}.

Author Contributions: Writing—original draft, J.-W.P.; Writing—review and editing, Y.-W.J. and J.S. All authors have read and agreed to the published version of the manuscript.

Funding: The research was supported by Wonkwang University in 2022.

Data Availability Statement: The original contributions presented in the study are included in the article. Further inquiries can be directed to the corresponding author.

Conflicts of Interest: The authors declare no conflict of interest.

References

1. Carrette, L.; Friedrich, K.A.; Stimming, U. Fuel cells-fundamentals and applications. *Fuel Cells* **2001**, *1*, 5–39. [CrossRef]
2. Stambouli, A.B.; Traversa, E. Solid oxide fuel cells (SOFCs): A review of an environmentally clean and efficient source of energy. *Renew. Sustain. Energy Rev.* **2022**, *6*, 433–455. [CrossRef]
3. Gupta, S.; Kellogg, W.; Xu, H.; Liu, X.; Cho, J.; Wu, G. Bifunctional Perovskite Oxide Catalysts for Oxygen Reduction and Evolution in Alkaline Media. *Chem.–Asian J.* **2016**, *11*, 10–21. [CrossRef]
4. Kim, K.; Lopez, K.J.; Sun, H.J.; An, J.C.; Park, G.; Shim, J. Electrochemical performance of bifunctional Co/graphitic carbon catalysts prepared from metal-organic frameworks for oxygen reduction and evolution reactions in alkaline solution. *J. Appl. Electrochem.* **2018**, *48*, 1231–1241. [CrossRef]
5. Lu, L.; Zheng, Y.; Yang, R.; Kakimov, A.; Li, X. Recent advances of layered double hydroxides-based bifunctional electrocatalysts for ORR and OER. *Mater. Today Chem.* **2021**, *21*, 100488. [CrossRef]
6. Liu, M.; Zhao, Z.; Duan, X.; Huang, Y. Nanoscale Structure Design for High-Performance Pt-Based ORR Catalysts. *Adv. Mater.* **2019**, *31*, 1802234. [CrossRef]
7. Wu, M.; Wang, Y.; Wei, Z.; Wang, L.; Zhuo, M.; Zhang, J.; Han, X.; Ma, J. Ternary doped porous carbon nanofibers with excellent ORR and OER performance for zinc-air batteries. *J. Mater. Chem. A* **2018**, *6*, 10918–10925. [CrossRef]
8. Stoerzinger, K.A.; Risch, M.; Han, B.; Shao-Horn, Y. Recent Insights into Manganese Oxides in Catalyzing Oxygen Reduction Kinetics. *ACS Catal.* **2015**, *5*, 6021–6031. [CrossRef]
9. Wang, Y.J.; Long, W.; Wang, L.; Yuan, R.; Ignaszak, A.; Fang, B.; Wilkinson, D.P. Unlocking the door to highly active ORR catalysts for PEMFC applications; polyhedron-engineered Pt-based nanocrystals. *Energy Environ. Sci.* **2018**, *11*, 258–275. [CrossRef]
10. Kim, H.Y.; Ju, Y.W. Fabrication of Mn-N-C Catalyst for Oxygen Reduction Reactions Using Mn-Embedded Carbon Nanofiber. *Energies* **2020**, *13*, 2561. [CrossRef]

11. Reier, T.; Oezaslan, M.; Strasser, P. Electrocatalytic Oxygen Evolution Reaction (OER) on Ru, Ir, and Pt Catalysts: A Comparative Study of Nanoparticles and Bulk Materials. *ACS Catal.* **2012**, *2*, 1765–1772. [CrossRef]
12. Byon, H.R.; Suntivich, J.; Shao-Horn, Y. Graphene-Based Non-Noble-Metal Catalysts for Oxygen Reduction Reaction in Acid. *Chem. Mater.* **2011**, *23*, 3421–3428. [CrossRef]
13. Gorlin, Y.; Chung, C.J.; Nordlund, D.; Clemens, B.M.; Jaramillo, T.F. Mn_3O_4 Supported on Glassy Carbon: An Active Non-Precious Metal Catalyst for the Oxygen Reduction Reaction. *ACS Catal.* **2012**, *2*, 2687–2694. [CrossRef]
14. Prabu, M.; Ketpang, K.; Shanmugam, S. Hierarchical nanostructured $NiCo_2O_4$ as an efficient bifunctional non-precious metal catalyst for rechargeable zinc-air batteries. *Nanoscale* **2014**, *6*, 3173–3181. [CrossRef]
15. Wang, J.; Kong, H.; Zhang, J.; Hao, Y.; Shao, Z.; Ciucci, F. Carbon-based electrocatalysts for sustainable energy applications. *Prog. Mater. Sci.* **2021**, *116*, 100717. [CrossRef]
16. Zhang, J.; Zhang, T.; Ma, J.; Wang, Z.; Liu, J.; Gong, X. ORR and OER of Co-N codoped carbon-based electrocatalysts enhanced by boundary layer oxygen molecules transfer. *Carbon* **2021**, *172*, 556–568. [CrossRef]
17. Fu, G.; Tang, Y.; Lee, J.M. Recent advances in carbon-based bifunctional oxygen electrocatalysts for Zn-air batteries. *ChemElectroChem* **2018**, *5*, 1424–1434. [CrossRef]
18. Béjar, J.; Álvarez-Contreras, L.; Ledesma-García, J.; Arjona, N.; Arriaga, L.G. Electrocatalytic evaluation of Co_3O_4 and $NiCo_2O_4$ rosettes-like hierarchical spinel as bifunctional materials for oxygen evolution (OER) and reduction (ORR) reactions in alkaline media. *J. Electroanal. Chem.* **2019**, *847*, 113190. [CrossRef]
19. Zhou, L.; Deng, B.; Jiang, Z.; Jiang, Z.J. Shell thickness controlled core-shell Fe_3O_4@CoO nanocrystals as efficient bifunctional catalysts for the oxygen reduction and evolution reactions. *Chem. Commun.* **2019**, *55*, 525–528. [CrossRef]
20. Wang, Q.; Xue, Y.; Sun, S.; Li, S.; Miao, H.; Liu, Z. $La_{0.8}Sr_{0.2}Co_{1-x}Mn_xO_3$ perovskites as efficient bi-functional cathode catalysts for rechargeable zinc-air batteries. *Electrochim. Acta* **2017**, *254*, 14–24. [CrossRef]
21. Wang, H.; Zhou, M.; Choudhury, P.; Luo, H. Perovskite oxides as bifunctional oxygen electrocatalysts for oxygen evolution/reduction reactions-A mini review. *Appl. Mater. Today* **2016**, *16*, 56–71. [CrossRef]
22. Kim, H.Y.; Ju, Y.W. Influence of cobalt dopant in $NiFe_{2-x}Co_xO_4$ ($0 \leq x \leq 2$) on electrochemical catalytic properties. *Int. J. Hydrogen Energy* **2021**, *46*, 38191–38197. [CrossRef]
23. Wu, G.; Zelenay, P. Nanostructured nonprecious metal catalysts for oxygen reduction reaction. *Acc. Chem. Res.* **2013**, *46*, 1878–1889. [CrossRef] [PubMed]
24. Wu, G.; More, K.L.; Johnston, C.M.; Zelenay, P. High-performance electrocatalysts for oxygen reduction derived from polyaniline, iron, and cobalt. *Science* **2011**, *332*, 443–447. [CrossRef] [PubMed]
25. Xu, X.; Wang, W.; Zhou, W.; Shao, Z. Recent advances in novel nanostructuring methods of perovskite electrocatalysts for energy-related applications. *Small Methods* **2018**, *2*, 180071. [CrossRef]
26. Yan, L.; Lin, Y.; Yu, X.; Xu, W.; Salas, T.; Smallidge, H.; Zhou, M.; Luo, H. $La_{0.8}Sr_{0.2}MnO_3$-Based Perovskite Nanoparticles with the A-site Deficiency as High Performance Bifunctional Oxygen Catalyst in Alkaline Solution. *ACS Appl. Mater. Interfaces* **2017**, *9*, 23820–23827. [CrossRef]
27. Xu, X.; Pan, Y.; Ge, L.; Chen, Y.; Mao, X.; Guan, D.; Li, M.; Zhong, Y.; Hu, Z.; Peterson, V.K.; et al. High-Performance Perovskite Composite Electrocatalysts Enabled by Controllable Interface Engineering. *Small* **2021**, *17*, 2101573. [CrossRef]
28. Zhou, W.; Sunarso, J. Enhancing Bi-functional Electrocatalytic Activity of Perovskite by Temperature Shock: A Case Study of $LaNiO_{3-\delta}$. *J. Phys. Chem. Lett.* **2013**, *4*, 2982–2988. [CrossRef]
29. Sun, J.; Du, L.; Sun, B.; Han, G.; Ma, Y.; Wang, J.; Huo, H.; Zuo, P.; Du, C.; Yin, G. A bifunctional perovskite oxide catalyst: The triggered oxygen reduction/evolution electrocatalysis by moderate Mn-Ni co-doping. *J. Energy Chem.* **2021**, *54*, 217–224. [CrossRef]
30. Zhao, Y.; Hang, Y.; Zhang, Y.; Wang, Z.; Yao, Y.; He, X.; Zhang, C.; Zhang, D. Strontium-doped perovskite oxide $La_{1-x}Sr_xMnO_3$ (x = 0, 0.2, 0.6) as a highly efficient electrocatalyst for nanoqueous Li-O_2 batteries. *Electrochim. Acta* **2017**, *232*, 296–302. [CrossRef]
31. Bhattar, S.; Abedin, M.A.; Kanikar, S.; Spivey, J.J. A review on dry reforming of methane over perovskite derived catalysts. *Catal. Today* **2021**, *365*, 2–23. [CrossRef]
32. Bu, Y.; Nam, G.; Kim, S.; Choi, K.; Zhong, Q.; Lee, J.; Qin, Y.; Cho, J.; Kim, G. A tailored Bifunctional Electrocatalyst: Boosting Oxygen Reduction/Evolution Catalysis via Electron Transfer Between N-Doped Graphene and Perovskite Oxides. *Small* **2018**, *14*, 1802767. [CrossRef]
33. Chen, J.; Shen, M.; Wang, X.; Wang, J.; Su, Y.; Zhao, Z. Catalytic performance of NO oxidation over $LaMeO_3$ (Me = Mn, Fe, Co) perovskite prepared by the sol-gel method. *Catal. Commun.* **2013**, *37*, 105–108. [CrossRef]
34. Navas, D.; Fuentes, S.; Castro-Alvarez, A.; Chavez-Angel, E. Review on sol-gel synthesis of perovskite and oxide nanomaterials. *Gels* **2021**, *7*, 275. [CrossRef]
35. Walton, R.I. Perovskite oxides prepared by hydrothermal and solvothermal synthesis: A review of crystallization, chemistry, and compositions. *Chem. Eur. J.* **2020**, *26*, 9041–9069. [CrossRef]
36. Kim, H.Y.; Shin, J.; Jang, I.C.; Ju, Y.W. Hydrothermal Synthesis of Three-Dimensional Perovskite $NiMnO_3$ Oxide and Application in Supercapacitor Electrode. *Energies* **2019**, *13*, 36. [CrossRef]
37. Nguyen, T.A.; Pham, V.N.; Le, H.T.; Chau, D.H.; Mittova, V.O.; Nguyen, L.T.T.; Dinh, D.A.; Hao, T.V.N.; Mittova, I.Y. Cystal structure and magnetic properties of $LaFe_{1-x}Ni_xO_3$ nanomaterials prepared via a simple co-precipitation method. *Ceram. Int.* **2019**, *45*, 21768–21772. [CrossRef]

38. Wang, W.; Lin, B.; Zhang, H.; Sun, Y.; Zhang, X.; Yang, H. Synthesis, morphology and electrochemical performances of perovskite-type oxide $La_xSr_{1-x}FeO_3$ nanofibers prepared by electrospinning. *J. Phys. Chem. Solids* **2019**, *124*, 144–150. [CrossRef]
39. Bian, J.; Su, R.; Yao, Y.; Wang, J.; Zhou, J.; Li, F.; Wang, Z.L.; Sun, C. Mg doped perovskite $LaNiO_3$ nanofibers as an efficient bifunctional catalyst for rechargeable zinc–air batteries. *ACS Appl. Energy Mater.* **2019**, *2*, 923–931. [CrossRef]
40. Hu, Q.; Yue, B.; Yang, D.; Zhang, Z.; Wang, Y.; Liu, J. Electrochemical and magnetic properties of electrospun $SmFeO_3$ and $SmCoO_3$ nanofibers. *J. Am. Ceram. Soc.* **2022**, *105*, 1149–1158. [CrossRef]
41. Kolahalam, L.A.; Viswanath, I.K.; Diwakar, B.S.; Govindh, B.; Reddy, V.; Murthy, Y.L.N. Review on nanomaterials: Synthesis and applications. *Mater. Today* **2019**, *18*, 2182–2190. [CrossRef]
42. Lou, X.W.; Archer, L.A.; Yang, Z. Hollow micro-/nanostructures: Synthesis and applications. *Adv. Mater.* **2008**, *20*, 3987–4019. [CrossRef]
43. Yoon, K.R.; Lee, G.Y.; Jung, J.W.; Kim, N.H.; Kim, S.O.; Kim, I.D. One-dimensional RuO_2/Mn_2O_3 hollow architectures as efficient bifunctional catalysts for lithium–oxygen batteries. *Nano Lett.* **2016**, *16*, 2076–2083. [CrossRef] [PubMed]
44. Peng, S.; Han, X.; Li, L.; Chou, S.; Ji, D.; Huang, H.; Du, Y.; Liu, J.; Ramakrishna, S. Electronic and defective engineering of electrospun $CaMnO_3$ nanotubes for enhanced oxygen electrocatalysis in rechargeable zinc–air batteries. *Adv. Energy Mater.* **2018**, *8*, 1800612. [CrossRef]
45. Mahmood, Q.; Afzal, A.; Siddiqi, H.M.; Habib, A. Sol–gel synthesis of tetragonal ZrO_2 nanoparticles stabilized by crystallite size and oxygen vacancies. *J. Sol-Gel Sci. Technol.* **2013**, *67*, 670–674. [CrossRef]
46. Zhou, Y.; Xie, M.; Song, Y.; Yan, D.; Wang, Z.; Zhang, S.; Deng, C. Edge-enriched Ni-N_4 atomic sites embedded enoki-mushroom-like carbon nanotubes assembling hollow fibers for CO_2 conversion and flexible Zn-air battery. *Energy Storage Mater.* **2022**, *47*, 235–248. [CrossRef]
47. Chen, Y.; Bu, Y.; Zhao, B.; Zhang, Y.; Ding, D.; Hu, R.; Weo, T.; Rainwater, B.; Ding, Y.; Chen, F.; et al. A durable, high-performance hollow-nanofiber cathode for intermediate-temperature fuel cells. *Nano Energy* **2016**, *26*, 90–99. [CrossRef]
48. Merino, N.A.; Barbero, B.P.; Eloy, P.; Cadús, L.E. $La_{1-x}Ca_xCoO_3$ perovskite-type oxides: Identification of the surface oxygen species by XPS. *Appl. Surf. Sci.* **2006**, *253*, 1489–1493. [CrossRef]
49. Hirai, S.; Morita, K.; Yasuoka, K.; Shibuya, T.; Tojo, Y.; Kamihara, Y.; Miura, A.; Suzuki, H.; Ohno, T.; Matsuda, T.; et al. Oxygen vacancy-originated highly active electrocatalysts for the oxygen evolution reaction. *J. Mater. Chem. A* **2018**, *6*, 15102–15109. [CrossRef]
50. Deng, Y.; Tian, X.; Shen, G.; Gao, Y.; Lin, C.; Ling, L.; Cheng, F.; Liao, S.; Zhang, S. Coupling hollow Fe_3O_4 nanoparticles with oxygen vacancy on mesoporous carbon as a high-efficiency ORR electrocatalyst for Zn-air battery. *J. Colloid Interface Sci.* **2020**, *567*, 410–418. [CrossRef]
51. Park, J.W.; Ju, Y.W. Evaluation of Bi-Functional Electrochemical Catalytic Activity of Co_3O_4-$CoFe_2O_4$ Composite Spinel Oxide. *Energies* **2022**, *16*, 173. [CrossRef]
52. Mahammed, A.; Gross, Z. Metallocorroles as electrocatalysts for the oxygen reduction reaction (ORR). *Isr. J. Chem.* **2016**, *56*, 756–762. [CrossRef]

Disclaimer/Publisher's Note: The statements, opinions and data contained in all publications are solely those of the individual author(s) and contributor(s) and not of MDPI and/or the editor(s). MDPI and/or the editor(s) disclaim responsibility for any injury to people or property resulting from any ideas, methods, instructions or products referred to in the content.